A Feature Fusion Airport Detection Method Based on the Whole Scene Multispectral Remote Sensing Images

Xinyu Dong [ID], Jia Tian, and Qingjiu Tian

Abstract—Being one of the most important infrastructures, airports play a vital role in both civil fields and military fields. However, detect airports directly based on the whole scene remote sensing images (RSIs) with complex background remains challenging. To address this issue, this article proposes a method that mainly combines spectral features and geometric features of airports with concrete runways to detect multiple airports simultaneously from a whole scene multispectral image with medium-high spatial resolution and with comparatively few bands (contains blue, green, red, and near-infrared bands). Specifically, a decision tree algorithm was developed based on the analysis of spectral features to extract main concrete areas within the whole RSI. Then, the geometric features are used to aim at extracting the point marks of candidate airports. The influence of different image spatial resolutions of the proposed method is explored and the detection effect and processing efficiency of proposed method is verified based on whole scene RSIs with complex background. The analysis of experimental results shows that Sentinel-2 images is more suitable for airport detection than Gaofen-6 and Landsat-8 images based on the proposed method. In addition, the proposed method provides high-accuracy detection of category IV airports based on Sentinel-2 images with different background complexity in experimental areas indicate the proposed method has a high robust and a good applicability. Finally, run-time test of the proposed method was conducted, and it demonstrates the proposed method has the higher processing efficiency when applying to regional airport detection.

Index Terms—Airport detection, concrete runways, decision tree, multispectral remote sensing, whole scene image.

I. INTRODUCTION

THE detection of man-made objects based on remote sensing images (RSIs) currently plays an important role in earth observation fields such as urban planning, geographic information systems, emergency response, and disaster relief [1], [2]. All such applications have benefited from the rapid development of remote sensing techniques, which have increased the quality and quantity of RSIs. As a typical man-made object, airports not only serve as fundamental transport infrastructure that promotes the economic development of their area but also serve a critical role in the military infrastructure for maintaining national or regional security and stability [3], [4]. Therefore, dynamic monitoring of airports requires an efficient method to directly detect airports from RSIs.

The airport detection focuses on how to locate the airports precisely under the condition of complex backgrounds. Numerous previous studies have proposed various approaches to detect airports from different RSIs, and we summarize those studies from two aspects: one concerns the RSIs used in previous research, and the other considers the development of methods for airport detection.

Although various types of remote sensing data may be used to detect man-made objects from RSIs, optical RSIs are typically used to detect airports [5]. One of the challenges of airport detection based on optical RSIs is the complex background conditions, which include man-made features such as the roads, buildings, and natural features such as the vegetation, bare soil. In most cases, studies have acquired true-color RSIs of multiple spatial resolutions from Google Earth [6]–[10]. The advantages of Google Earth images are that they are not only available free of charge but also offer high spatial resolution [11]. However, Google Earth images differ totally from the original RSIs due to their lack of band information. Consequently, the spectral information of the original remote sensing images is difficult to be used. Synthetic aperture radar images, however, can be acquired day or night, independent of lighting or weather conditions, so these data are also used in airport detection [5], [12]–[14]. The defect of SAR images lies in its relatively low spatial resolution and low signal-to-noise ratio. Moreover, several previous studies of airport detection have used medium and high spatial resolution RSIs, such as IKONOS images [15], Gaofen-1 images, Landsat-8 images [16], and Gaofen-2 images [17]. In fact, researchers seldom use aerial optical imagery for airport detection [18]. Overall, the optical RSIs used in mostly airport detection studies have been acquired from satellite platforms and thereby offer the advantage of wide range and high spatial resolution. Significantly, most of the previous studies of airport detection based on image block containing only a single airport. For the whole scene image, it

Xinyu Dong is with the International Institute for Earth System Science, Nanjing University, Nanjing 210023, China, with the Jiangsu Provincial Key Laboratory of Geographic Information Science and Technology, Nanjing University, Nanjing 210023, China, and also with the Collaborative Innovation Center for the South Sea Studies, Nanjing University, Nanjing 210093, China (e-mail: dg1827003@smail.nju.edu.cn).

Jia Tian and Qingjiu Tian are with the International Institute for Earth System Science, Nanjing University, Nanjing 210023, China, and also with the Jiangsu Provincial Key Laboratory of Geographic Information Science and Technology, Nanjing University, Nanjing 210023, China (e-mail: tianjia@nju.edu.cn; tianqj@nju.edu.cn).

usually contains multiple airports, and the spatial distribution is relatively scattered and does not have regularity, which makes the existing airport detection method difficult to be applied to airport detection based on the whole scene image as the processing unit. Although some researchers carry out airport detection mainly based on deep learning methods by using the large-scale images with high spatial resolution, there are still problems of slow efficiency [17], [19]. Therefore, it is necessary to make up for the low efficiency of airport detection based on the whole scene optical RSIs [17]. In addition, the impact of spatial resolution on airport detection needs to be further discussed and analyzed.

Previously developed methods of airport detection from RSIs could be divided into two groups. The first group, developed prior to 2016, used relatively traditional methods based on the remote sensing theory. This group may be further divided into two subcategories: The first subcategory contains geometric feature methods that are generally based on line or edge detection [20], whereas the second subcategory involves methods based on segmentation, which mainly exploits the airport texture [15], [21]. Since the runway is the most important area and discriminating feature of airports and occupies the majority of the airport area [22], the first subcategory focuses on airport runways by using edges or line segments to characterize the runways. These methods commonly include line-detect methods such as the Hough line transform (HLT) and the line-segment detector, which have been used to extract straight, parallel lines to detect airports [6], [8], [12], [13]. These methods could be relatively simple and rapid, but are commonly causing many false alarms by irrelevant objects of similar geometric structure, such as road networks [23]. However, the spectral information contained within RSIs has not been exploited in previous research. The materials of most airport runways are concrete and asphalt, which has remarkable spectral characteristics [24]. How to use the spectral characteristics of airport runways to assist in airport detection needs to be further discussed. The second subcategory of airport detection methods focuses on color or texture in local RSI segments; however, these methods tend to be excessively slow. RSI images can be segmented by using oriented-gradient histograms [25], the scale-invariant feature transform [15], [21], [26], or visual saliency [3], [7], [10], [27]. Background interference in satellite images is complex due to the different imaging mechanisms, although some interference becomes as salient as the extracted regions of interest (e.g., airports), which means that background interference cannot be suppressed when it is salient for detecting regions of interest [28].

The second group of airport detection methods (post-2016) mainly uses deep-learning methods [e.g., ResNet [29], convolutional neural networks [30], and fast region-based convolutional neural networks [16]] that integrate computer-vision methods and biological-vision mechanisms based on the rapid development of image-processing techniques. Deep learning is an automated feature-learning and representation framework that can learn deep features in RSIs [31]. In general, deep-learning algorithms require a large number of training samples that manually clipped and labeled based on original RSIs by professional researchers, which constitutes a heavy workload and makes for a slow process of pattern matching and sample training [32].

TABLE I
AERODROME REFERENCE CODE

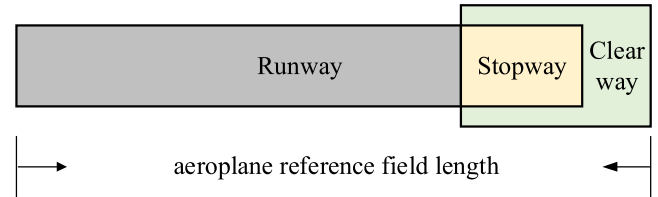| Element 1		Element 2		
Code Number	Aeroplane Reference Field Length (m)	Code Letter	Wingspan (m)	Outer Main Gear Wheel Span (m)
1	<800	A	<15	<4.5
2	800~1200	B	15~24	4.5~6
3	1200~1800	C	24~36	6~9
4	>1800	D	36~52	9~14
		E	52~65	9~14
		F	65~80	14~16

Fig. 1. Example of ARFL.

Furthermore, Some of the research involves indirect detection of airports by combining RSI-based deep-learning methods to detect aircraft in high spatial resolution RSIs [33]. Overall, the deep learning methods have its unique advantages, it is still challenging to directly detect airports within the whole scene middle-high spatial resolution RSIs.

Airfield area is a defined area for take-OFF, landing, taxiing, and parking of aircraft, including runway, strip, runway end safety zone, taxiway, apron, and the area around the airport with restrictions on obstacles [34]. To distinguish between airfield areas, Table I use the aerodrome reference code (ARC) of the International civil aviation organization (ICAO) [34]. The ARC gives the airport category, and the code is composed of two elements, which are related to the aeroplane performance characteristics and dimensions. And element 1 is a code number based on the aeroplane reference field length (ARFL). The ARFL is the minimum field length required for take-OFF at maximum certificated take-OFF mass, sea level, standard atmospheric conditions, still air, and zero runway slope. The ARFL includes the length of airport runway, stopway, and clearway (see Fig. 1). A stopway on which an aeroplane may be stopped in the event of an abandoned take-OFF may be provided at the end of a runway, and as wide as the width of its associated runway [35]. A clearway, consisting of an obstruction-free rectangular plane, may be provided at the end of a runway [35], but should not exceed half the length of the runway. The ARFL is not equal to the runway length. The ARFL is equal to the runway length where stopway and clearway are not provided. In other words, the runway length is less than or equal to the ARFL.

In fact, the surface of runway and stopway are sealed with a surface treatment, which may include asphalt or concrete. Due to the spatial resolution limitation of the satellite remote sensing images used in this article, the airports detected in this article are mainly aimed at the category IV airports, which ARFL are longer than 1800 m and runways are longer than 1200 m. In addition, the width of runway of category IV airports should be not less than 45 m [34].

We, thus, propose a feature fusion method to detect airports based on the whole scene multispectral RSIs with middle-high spatial resolution with the following considerations.

1) *Spectral features*. Runways are made mainly of concrete and asphalt. We consider herein only airports with concrete runways. The analysis of the spectral curve characteristics of typical objects within the RSI is conducted.
2) *Geometric features*. Airports are detected by using geometric features of runways such as area and line features.
3) *Scale features*. We detect airports based on the different RSIs and discuss the influence of spatial resolution for airport detection from RSIs.

The main contributions of this article are summarized as follows.

1) We develop a decision tree method to extract main concrete areas within whole scene images based on the surface reflectance analysis.
2) There are many line marks of airport are extracted based on the whole scene RSIs by combining the morphological operation method and the HLT method, which may confound the airport detect result. And we build a rule system to effectively select the unique line mark of each airport to identify possible airport target.
3) The proposed method for airport detection herein based on whole scene multiple spectral remote sensing images. Therefore, only fewer bands that contain blue, green, red, and near-infrared bands, which are common are used.

The rest of this article is organized as follows. Section II introduces the experiment area and the data used in this article. Section III describes the methodology of airport detection. Section IV describes the experimental setup, including the experimental parameters and the methods used to evaluate the results. The airport detection results are then analyzed and discussed, and their accuracy is evaluated. Finally, Section V concludes this article. And the Appendix shows the additional tables and figures.

II. EXPERIMENTAL AREA AND DATA

We first describe the experimental areas of this article, and then describe the essential information and introduce the preprocess of RSIs used in this article.

A. Experimental Areas

The study area contains 12 experimental areas located around the world by considering regional geographical location and geographical environment, as shown in Fig. 2, which produced by using the ArcGIS version 10.6 software (ESRI, Redlands, CA, USA). Therefore, the RSIs of all the experimental areas are having different complexity and geographical diversity. And the runways of the airports in the experimental areas are made mainly of concrete. Experimental area A in Beijing-Tianjin-Hebei region (BTH region), China, was selected to test the effect of the proposed method applied to RSIs acquired from Gaofen-6, Sentinel-2, and Landsat-8. And the influence of image spatial resolution on airport detection is further discussed. Then, the effectiveness of the proposed method was validated by combining with other experimental areas.
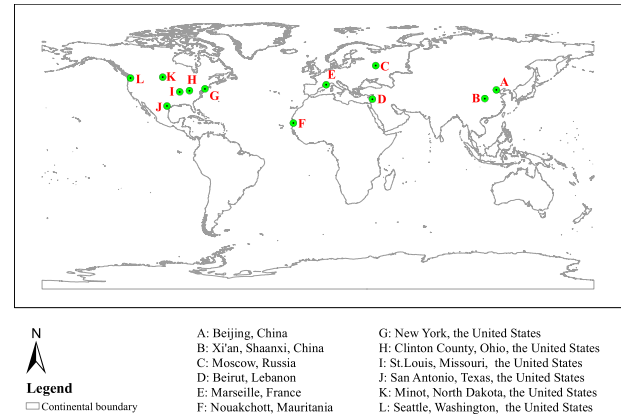

Fig. 2. Locations of experimental areas.

N

Legend
☐ Continental boundary

A: Beijing, China
B: Xi'an, Shaanxi, China
C: Moscow, Russia
D: Beirut, Lebanon
E: Marseille, France
F: Nouakchott, Mauritania

G: New York, the United States
H: Clinton County, Ohio, the United States
I: St.Louis, Missouri, the United States
J: San Antonio, Texas, the United States
K: Minot, North Dakota, the United States
L: Seattle, Washington, the United States

TABLE II
COMPARISON OF BASIC PARAMETERS OF DIFFERENT SATELLITES

Satellite	Sensor	SR	TR	SS	BN	DV
Gaofen-6	Multispectral camera	8	2	~90 × 99	4	~1.5
Sentinel-2	Multispectral Instrument	10	5	~110 × 110	13	~2.7
Landsat-8	Operational Land Imager	30	16	~195 × 190	7	~0.8

Note: SR represent spatial resolution in m. TR represent temporal resolution in day. SS represent scene size in km^2. BN represent band number. DV represent data volume in gigabyte.

TABLE III
BASIC INFORMATION FOR RSIs USED IN THIS ARTICLE

Country	Experiment location	Satellite	Acquisition Date
China	Beijing	Gaofen-6	15-Apr-2019
		Sentinel-2	12-May-2020
		Landsat-8	05-Nov-2019
	Xi'an		26-Aug-2020
Russia	Moscow		06-Jun-2019
Lebanon	Beirut		23-Aug-2020
Mauritania	Nouakchott		22-May-2020
France	Marseille		23-Jul-2020
	New York	Sentinel-2	25-Aug-2020
	St. Louis		16-Aug-2020
USA	Clinton County		08-Jun-2020
	San Antonio		13-Jul-2020
	Minot		11-Aug-2020
	Seattle		28-Aug-2020

B. RSI Data and Preprocessing

This article uses three different RSIs: Gaofen-6, Sentinel-2, and Landsat-8 (see Table II). Table III lists the basic information contained in each of the RSIs. Gaofen-6 is a high-spatial-resolution satellite launched by China in 2018, and it provides RSIs with the highest temporal resolution of the three satellites. This article uses data from the Gaofen-6 multispectral sensor with 8 m spatial resolution. The Gaofen-6 images were downloaded from the website of the China Center for Resources Satellite Date and Application,[1] and the ENVI version 5.3 (Exelis, Boulder, CO, USA) software was used for geometric and radiometric processing.

[1][Online]. Available: http://www.cresda.com/EN/

TABLE IV
ALBEDOS (REFLECTANCE) OF DIFFERENT PAVEMENT SURFACES

Pavement Materials	Albedo (New)	Albedo (Weathered)
asphalt	0.05 – 0.10	0.10 – 0.15
gray portland cement concrete	0.35 – 0.40	0.20 – 0.30
white portland cement concrete	0.70 – 0.80	0.40 – 0.60

TABLE V
STATISTICAL RESULTS FOR AIRPORT DETECTION

ID	Location	d	f	N_f	m	N
1	Beijing	5	1	0	6	6
2	Moscow	4	0	0	4	4
3	Clinton County	2	1	0	2	1
4	Nouakchott	1	0	0	1	1
5	Xi'an	2	1	0	3	2
6	Beirut	3	0	0	3	3
7	Marseille	3	2	0	5	3
8	New York	1	0	0	1	1
9	St. Louis	2	1	1	3	3
10	Minot	2	0	0	2	2
11	Seattle	1	0	0	1	1
12	San Antonio	1	3	2	4	3

TABLE VI
OVERALL ACCURACY OF AIRPORT DETECTION

Statistical Metrics	*ODR*	*FAR*	*MR*
Numerical Results	90.00%	25.71%	10.00%

The Sentinel-2 Level 2 bottom-of-atmosphere reflectance products were downloaded from Sentinel's Scientific Data Hub,[2] and no need additional preprocessing. The images were exported in the GeoTIFF format, which is based on the Sentinel Application Platform of the European Space Agency.

Finally, Landsat-8 images were downloaded from the USGS website.[3] These images have the lowest spatial resolution of the three satellites. The ENVI version 5.3 software was again used for the geometric, radiometric, and atmospheric corrections of the Landsat-8 images. In addition, we finished the charting of the study result using the ArcGIS version 10.6 software.

C. Auxiliary Data

To verify the accuracy of the proposed method, the airport validation data were downloaded from the OurAirports website[4] and used to acquire the airport locations within each RSI. OurAirports is a community-run website that provides datasets for collecting locations and descriptions of airports around the world. The airport information within the RSIs (Appendix Table IX) acquired from World Airport Codes[5] and Google Earth,[6] including the airport serial number, location, name, runway material, runway length, and width of the airport.

Fig. 3 shows the airports near Beijing. Four airports (B1–B4) appear in the Gaofen-6 image, seven airports (B1–B6) appear in

[2][Online]. Available: https://scihub.copernicus.eu/
[3][Online]. Available: https://earthexplorer.usgs.gov/
[4][Online]. Available: http://ourairports.com
[5][Online]. Available: www.world-airport-codes.com
[6][Online]. Available: www.Googleearth.com

TABLE VII
PROCESSING TIME OF PROPOSED METHOD APPLIED TO DIFFERENT REMOTE SENSING IMAGES

Experimental Area	Satellite Image	Acquisition Date	Run-Time (s)
Beijing	Gaofen-6	2019/4/15	145.677
	Sentinel-2	2020/5/12	85.704
	Landsat-8	2019/12/5	58.747
Xi'an		2019/12/6	77.879
Moscow		2019/12/7	69.611
Beirut		2019/12/8	81.671
Nouakchott		2019/12/9	68.588
Marseille		2019/12/10	99.411
New York	Sentinel-2	2019/12/11	68.888
St. Louis		2019/12/12	73.173
Clinton County		2019/12/13	72.109
San Antonio		2019/12/14	76.994
Minot		2019/12/15	65.686
Seattle		2019/12/16	68.747

TABLE VIII
COMPARISON OF DIFFERENT AIRPORT DETECTION METHODS

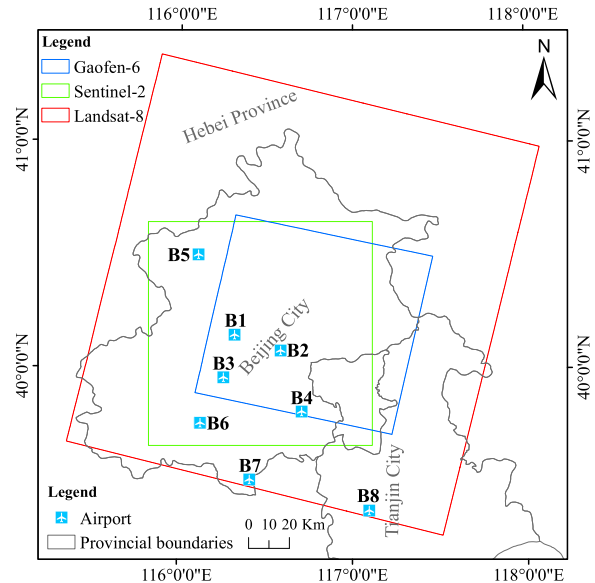| Method	Processing Efficiency
The propose method	0.6~1.2
Li et al.	19.1
Manual visual search method	373.7

Fig. 3. Airport locations and the extent of the three RSIs in BTH region.

the Sentinel-2 image, and nine airports (B1–B8) appear in the Landsat-8 image.

III. METHODOLOGY

Fig. 4 shows a flowchart describing the procedure proposed to detect airports from the whole scene multispectral RSIs. The procedure has six steps as follows.

1) The RSI surface reflectance is generated after image pre-processing.
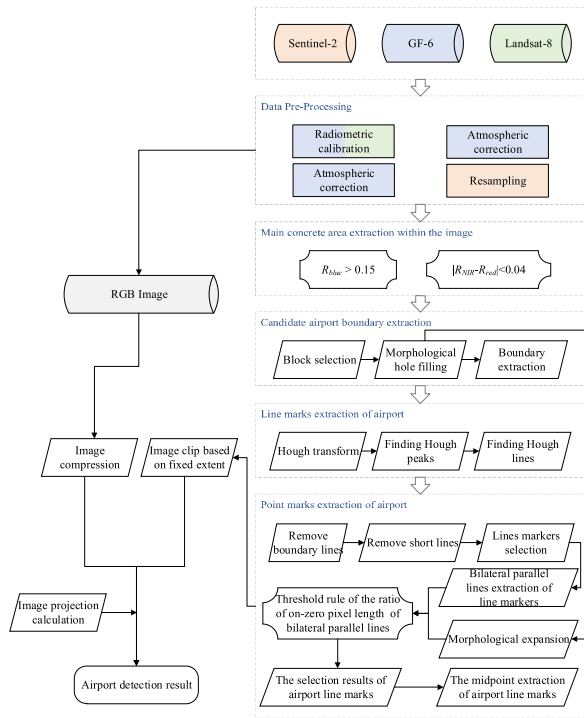2) Main concrete areas within the RSIs are extracted based on the decision tree algorithm.

Fig. 4.   Flowchart of the proposed method.

3) Morphological operation, including region filtering and hole filling, is then undertaken to extract the boundaries of candidate airports.

4) The HLT is used to extract the line marks of the candidate airports and to mark the possible airport targets.

5) The line marks are selected through building the rule system, then the central coordinates of the unique line marks are generated and serve as the point marks of airports.

6) Finally, the results of the airport detection are clipped by setting a fixed extent around the point marks based on the RGB RSIs. And all the results of airport detection contain corresponding geographical coordinates information.

Except for data preprocessing, all these steps were coded in Matlab Campus Edition run automatically on a desktop computer with an IntelCore i7-8700 central processing unit and 16 GB of random-access memory.

A. Extraction of Main Concrete Area Based on the Decision Tree Method

The spectral features of the images are now considered extracting concrete areas from the images. By drawing the spectral curves, we analyze the spectral characteristics of typical objects within the different RSIs. The decision tree algorithm is then developed for extracting the concrete area from the complete RSI.

1) Spectral Characteristics Analysis of Typical Objects in RSIs With Different Spatial Resolutions: Efficient extraction based on spectral information of man-made objects from RSIs with complex backgrounds is difficult because different types of objects within RSI may have similar spectral characteristics. The
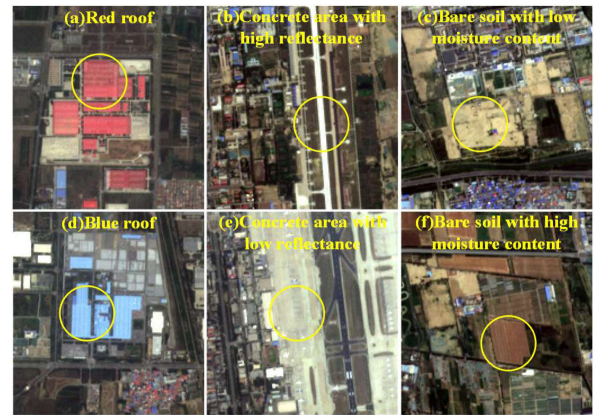

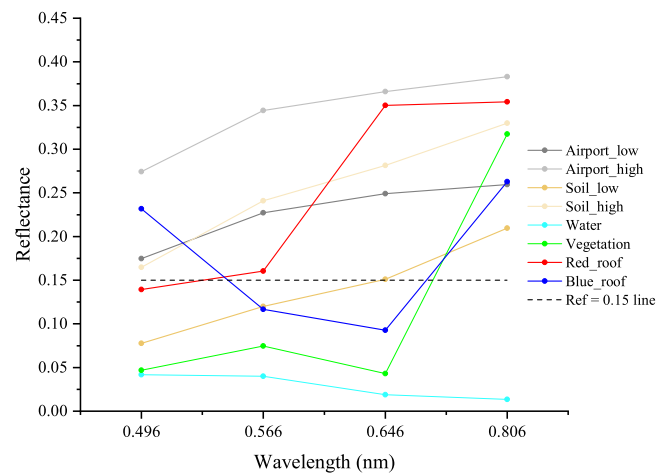Fig. 5.   Examples of typical objects (from Sentinel-2).

Fig. 6.   Gaofen-6 surface reflectance spectra from typical objects.

most common objects within RSI typically contain vegetation, water, bare soil, and impervious areas (e.g., buildings, roads). As shown in Fig. 5, buildings with red roofs and the blue roofs are very typical and have distinctive spectral characteristics. We, thus, select for analysis, in addition to areas of vegetation and water, red roofs [see Fig. 5(a)], blue roofs [see Fig. 5(d)], airport runways (concrete) with a high reflectance [see Fig. 5(b)] and low reflectance that may cause by weathering effect and abrasion [see Fig. 5(e)], bare soil with low moisture content [see Fig. 5(c)] and high moisture content [see Fig. 5(f)], and the lower the moisture content, the higher the reflectance.

Figs. 6–8 show the surface reflectance curve of typical objects taken from the Gaofen-6, Sentinel-2, and Landsat-8 images, respectively, using the surface reflectance in the blue, green, red, and NIR bands. The reflectance spectra of the objects in the three RSIs are similar, despite the different spectral response functions of the satellite sensors [36]. Note that extracting concrete objects is difficult because the reflectance of concrete objects is similar to that of bare soil.

Water has low absorption in the visible range; i.e., the transmission in the blue and green bands are relatively high, which leads to low reflectance in the blue band. Vegetation produces two chlorophyll absorption peaks, one each in the blue
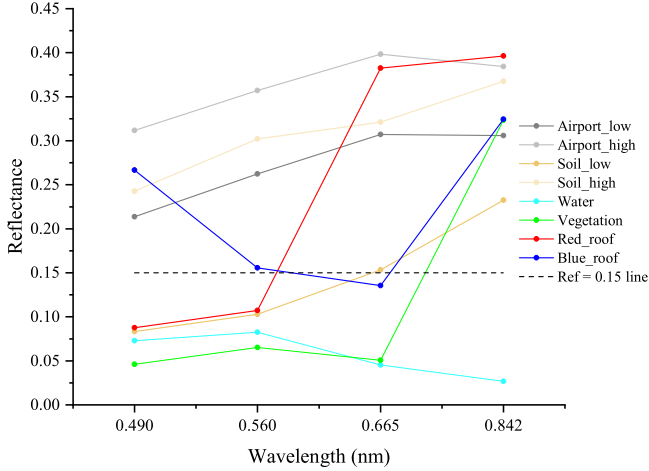
Fig. 7. Sentinel-2 surface reflectance spectra from typical objects.
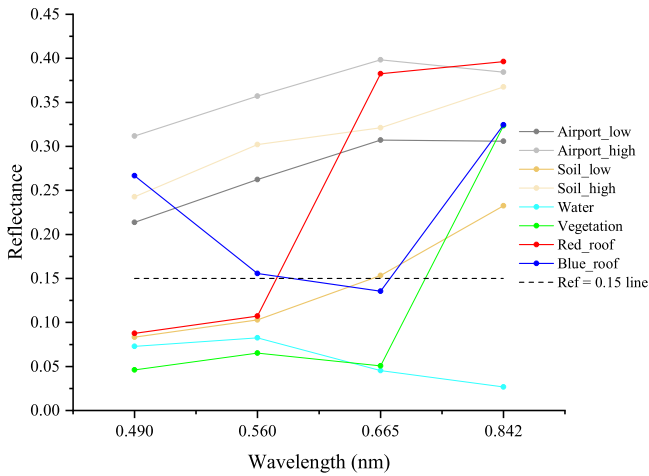

Fig. 8. Sentinel-2 surface reflectance spectra from typical objects.

Fig. 9. Decision tree algorithm for extracting concrete objects.

and green bands. Vegetation, thus, has low reflectance in the blue and green bands. Moreover, red-edge phenomena between the red and NIR bands lead to high reflectance between these bands. The different reflectance characteristics of bare soil may be due to the different soil moisture content, the reflectance decreases as soil moisture content increases [37]. The red roofs reflect strongly in the red and NIR bands and poorly in the blue and green bands, but the blue roofs are the opposite. Figs. 6–8 represent the concrete areas exhibit high reflectivity in the VNIR region.

2) Construction of Band Decision Tree Method for Extracting Main Concrete Area: The decision tree algorithm is applied in a stepwise manner to extract certain objects. For example, concrete areas are extracted only if a given area satisfies all the decision rules for concrete areas. Some natural objects such as vegetation or water is easy to extract or distinguish based on band indices (e.g., the normalized difference vegetation index [38], or the normalized difference water index [39]), whereas concrete objects are difficult to extract by designing these simple band indices. One reason for this situation is that the various man-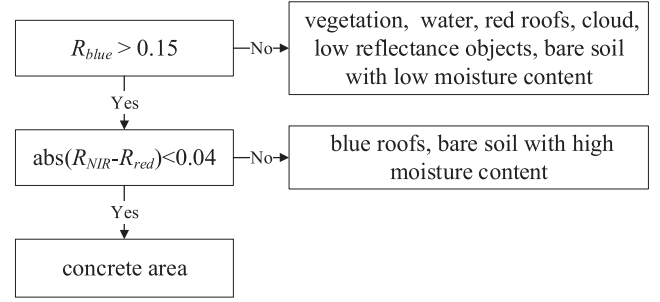made objects may have different spectral features due to their different surface materials. In addition, the computational efficiency may be improved by applying the decision tree rather than by using band indices. To extract concrete areas in the RSIs include concrete airport runways, decision tree algorithm was developed by analyzing the surface reflectance of different objects (see Fig. 9). After this processing stage, a binary result is generated that contains mainly concrete areas.

The reflectance threshold of blue band refers to the ground surface albedo (reflectance) of pavement materials measured by the American Concrete Pavement Association (American Concrete Pavement Association, 2002). The field measure is considered three types pavement surface materials in two cases of the new and weathered (see Table IV). And the measurement results show that the maximum reflectance of asphalt is 0.15 and the minimum reflectance of concrete is 0.20. In addition, the Figs. 6–8 shows that the concrete objects have the minimum reflectance in blue band among the VNIR bands. Hereafter, combining the spectral characteristics among the different typical objects (cf., dashed line in Figs. 6–8), we set the reflectance threshold of blue band equal to 0.15 to effectively distinguish the asphalt and concrete objects. Meanwhile, this threshold could also be used to remove vegetation, water, and red roof since their unique spectral characteristics in blue band that explained in the Section III-A1. In addition, the blue band has the spectral characteristics that is highly reflected by clouds and snow [40], [41], so the threshold could also remove the clouds within the RSIs.

After the processing of the $R_{\rm blue} > 0.15$, it generates the result mainly contains concrete areas, blue roofs, and bare soil with high moisture content. In fact, when the absolute value of the difference in reflectance between the red and NIR bands is less than 0.04 (cf., dashed line in Fig. 10), the nonconcrete areas can be further removed effectively.

B. Boundary Extraction of Candidate Airport Area Based on Mathematical Morphology

This section presents a series of mathematical morphology methods that are used to extracted candidate airport areas based on the geometric features of airports.

1) Selection of Suspected Airport Targets: Through the selection to remove the interference of nonairport targets based on the main concrete area extraction result. The "*bwareafilt*" function in MATLAB is used to remove large-area polygons
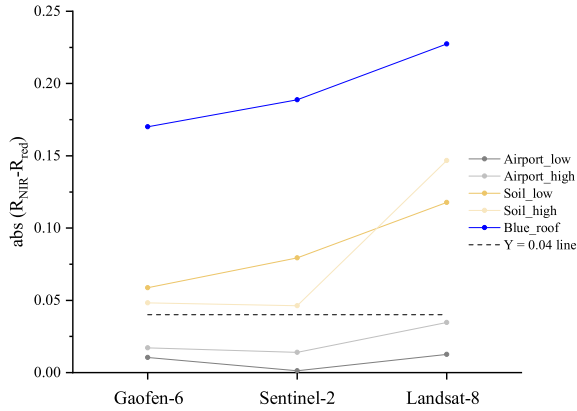
Fig. 10. Absolute differences value of reflectance between NIR and red of different typical objects among Gaofen-6, Sentinel-2, and Landsat-8 images.

Fig. 11. Hough transform: left graph is in Cartesian space; right graph is in Hough parameter space.

and small-area polygons. Polygons within a minimum-area threshold ($AT_{\min}$) and a maximum-area threshold ($AT_{\max}$) are candidate airport area.

Ideally, the concrete runways area of category IV airports are at least greater than the length of runway (1200 m) multiplies the width of runway (45 m). The $AT_{\min}$ is a threshold that determined by referring the area and considering the different spatial resolution of different remote sensing images.

The $AT_{\max}$ is determined by referring the concrete area of the Beijing Daxing International Airport, which is the biggest airport in the world. To eliminating interference of possible large concrete area that does not locate in airport area, it is necessary to set an upper limit value ($AT_{\max}$) to further distinguish airport and nonairport.

The $AT_{\min}$ and $AT_{\max}$ are fine-tuned to make it better suited to extracting concrete area of airports based on different spatial resolution images.

2) Candidate Airport Area Extraction: After region filtering, the candidate airport area extraction results are obtained. However, due to the existence of holes in the target and incomplete boundary connection, it needs to be further optimized. Therefore, the "*imfill*" function in MATLAB is used to fill the internal holes of the candidate airport area in the binary image, so as to obtain a more complete candidate airport area.

3) Extraction of Candidate Airport Boundaries: Based on the candidate airport area extraction after applying morphological hole filling, then use the MATLAB function "*bwperim*" to generate a binary image as candidate airport boundaries.

C. Line Marks Extraction of Candidate Airport Based on Hough Line Transform

The main purpose of this step is to obtain a unique set of point coordinates for each airport within the RSIs. To begin, the HLT is applied to find the lines within the candidate airport areas defined by the candidate airport perimeters. Next, the point coordinates of the airports are calculated after filtering the line marks within the airports.

Since airport runways have identifiable line characteristic, this characteristic can be used to identify airports. The Hough
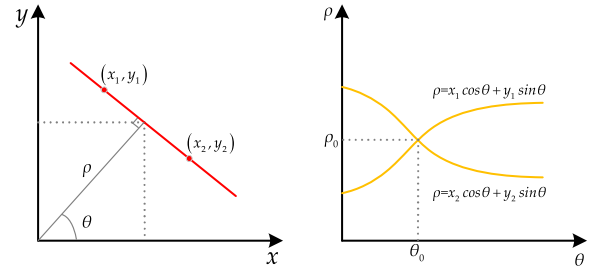
transform (HT) was first introduced by Hough [42] and can be used to detect lines, circles, or other parametric curves. It is already widely used in image processing. The basic theory behind the HT is that it detects peaks in a Hough parameter space to detect objects in binary images [43]. The HLT consist of three steps: the HT, finding the Hough peaks, and then finding the Hough lines.

Given a binary edge image A, the HT detects straight lines in A by mapping the Cartesian feature points in physical space to the Hough parameter space [44]. The points (x_i, y_i) in the line are transformed into Hough parameter space (θ, ρ) by using

$$\rho = x \cos \theta + y \sin \theta \tag{1}$$

where ρ is the shortest distance from the origin to the line containing (x_i, y_i), and θ is the angle between the x-axis and the vector $\vec{\rho}$. Fig. 11 shows the point in Cartesian spatial space and Hough-parameter. The HT generates a parameter space matrix whose rows and columns correspond to the θ and ρ values, respectively. Finding Hough peaks is equivalent to finding peaks in the Hough parameter space that represent potential lines in the binary image, and finding Hough lines is equivalent to finding the endpoints of the line segments corresponding to peaks in the HT.

D. Point Marks Extraction of Airports

The line marks generated by HLT are complex and diverse. In order to obtain the line marks within the airport area, it is necessary to establish certain rules to select the line marks. The specific implementation processes mainly include the following aspects.

1) Remove the Line Marks Near the Edge of Image: This kind of line mark is generally in the range of nonairport area. It could be removed by establishing the threshold rules combine the coordinate position of the end point of the line mark and the image extent. Assuming that the coordinates of the two end points of the line mark are $A(x_1, y_1)$ and $B(x_2, y_2)$, respectively, the number of image rows and columns are N_{row} and N_{column}, respectively. The weight factor f of the establishment rules is set to 0.001, which means when the line mark is within the range of a rectangle with the image boundary as the long side and the width is equal to one thousandth of the image size, it will be
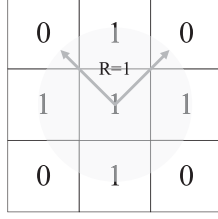
Fig. 12. Diagram of structuring element.

Fig. 13. Diagram of structuring element.

removed. The establishment rules are as follows:

$$\begin{cases} x_1 < \text{round}(N_{\text{row}} \times f) || x_1 > \text{round}\left[N_{\text{row}} \times (1-f)\right] \\ x_2 < \text{round}(N_{\text{row}} \times f) || x_2 > \text{round}\left[N_{\text{row}} \times (1-f)\right] \\ y_1 < \text{round}(N_{\text{column}} \times f) || y_1 > \text{round}\left[N_{\text{column}} \times (1-f)\right] \\ y_2 < \text{round}(N_{\text{column}} \times f) || y_2 > \text{round}\left[N_{\text{column}} \times (1-f)\right]. \end{cases} \tag{2}$$

2) Remove the Short Line Marks: The runway of the airport has a certain length, especially for the category IV airports, the runway length is more than 1200 m. Therefore, the short line marks within the whole scene image are removed by applying the minimum length threshold ($L_{\min}$), which is based on the runway length of category IV airports.

3) Line Marks Selection Based on Distance Threshold: There are multiple line marks extracted within an airport when it has multiple runways. And the distance between these line marks is close to each other, which will cause redundancy. In fact, the range of the airport is limited, and the distance between runways is also limited. Therefore, we set a reasonable distance threshold D_l between line marks by calculating the distance d_l between the midpoint of line marks. All the line marks are classified based on the distance rule $d_l < D_l$, and the maximum length line marks in each category is saved as the unique line marks of airports.

4) Remove Nonairport Line Marks: A threshold rule of the ratio of nonzero pixel of bilateral parallel lines is established to remove nonairport line marks.

First, morphological dilation is carried out based on the candidate airport area extraction result. Morphological dilation is one of the fundamental operators of grayscale mathematical morphology [45]. This step focuses on expanding objects according to a kernel called a "structuring element," which is defined as a binary mask of a given shape [46]. Given the input image A and the structuring element B, the dilation of A by B is defined as

$$A \oplus B = \left\{ z \Big| \left(\hat{B}\right)_z \cap A \neq \emptyset \right\}. \tag{3}$$

Fig. 12 shows a diagram of the structuring element B used in this step and which is defined as structuring element = strel (disk, 1). The operation creates a flat, disk-shaped structuring element.

The airport runway line marks extracted by HLT is located at the edge of one side of the airport runway. After processing of steps 1), 2), and 3), there are some extracted line marks are regarded as the error that not located within the airport area. Hence, we defined two same length lines that parallel with the line mark, as shown in Fig. 13. The blue line represents the line mark of airport, and the red lines represents the parallel lines of line mark. In this article, d is a fixed value and set to 2, which represents two pixels.
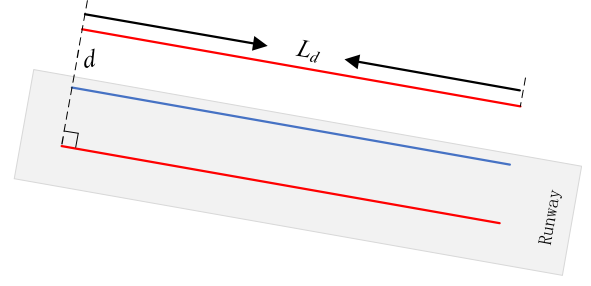
Then, the number of nonzero pixels of the parallel lines on both sides of the line marks are counted. And the number of nonzero pixels of the left parallel line is N_{l_z}, the number of nonzero pixels of the right parallel line is N_{r_z}, the number of the pixels of the line marks is L_d. The number of pixels is the length of the lines. And establish the threshold rule as follows:

$$\begin{cases} N_{l\_z}/L_d > 0.85 \text{ and } N_{r\_z}/L_d < 0.25 \\ N_{r\_z}/L_d > 0.85 \text{ and } N_{l\_z}/L_d < 0.25 \end{cases}. \tag{4}$$

The calculation formula of L_d as follows:

$$L_d = \sqrt{(x_1 - x_2)^\wedge 2 + (y_1 - y_2)^\wedge 2}. \tag{5}$$

The ratio of 0.85 and 0.25 are the optimal thresholds determined based on trial-and-error method, and has good general applicability.

E. Result Generation of the Airport Detection

After determining the airport point marks for an entire RSI, the detected airports are clipped by using a set of fixed square areas centered on the airport point marks in the RGB image from the original RSI. And the square areas had dimensions of fixed pixels (F_{pix}) for the Gaofen-6, Sentinel-2, and Landsat-8 images.

When saved in MATLAB, the 16-bit depth of the original RGB images could cause color distortion. In this case, the original RGB image was compressed without loss to generate 8-bit images based on the histogram statistics.

Assuming the image $B(i, j)$, the image compression calculation processing is as follows.

First, the minimum gray value $g_{\min}$ in the image B was obtained, and the number of pixels in the image whose gray value is not equal 0 and greater than $g_{\min}$ is C.

Then, the frequency of pixels with different gray value are counted, expressed as $h(x)$, and h represents the total number of pixels with gray value of x. The gray value p satisfying (6) was taken as the lower limit of the gray value, and the gray value q satisfying (7) was taken as the upper limit of the gray value

$$[h(p) + h(p-1) \geq C \times 0.02]$$
$$\text{and } [h(p-1) + h(p-2) \leq C \times 0.02] \tag{6}$$

$$[h(q) + h(q-1) \geq C \times 0.98]$$
$$\text{and } [h(q-1) + h(q-2) \leq C \times 0.98]. \tag{7}$$

Finally, the result $b(i, j)$ of compressed image was generated by calculating (8) based on the gray value of original image

$$\begin{cases} b'(i,j) = p, b(i,j) < p \\ b'(i,j) = \frac{b(i,j)-p}{(q-p)/255}, p \le b(i,j) \le q \\ b'(i,j) = q, b(i,j) > q. \end{cases} \quad (8)$$

In addition, the image coordinates information of each clipped airport detection result was recalculated, all the airport detection result were exported with projection coordinate information.

IV. ANALYSIS AND DISCUSSION OF EXPERIMENTAL RESULT

To verify the effectiveness and accuracy of the proposed method, we now evaluate the results of airport detection. In this section, the experimental parameters are described, and the experimental results are presented and discussed.

A. Experimental Setup

1) Setting Experimental Parameters: The threshold areas $AT_{\min}$ and $AT_{\max}$ mentioned in Section III-B1 play a vital role in the proposed method of extracting candidate airport areas. If $AT_{\min}$ is too big or $AT_{\max}$ is too small, some airports could be missed. In this article, $AT_{\max}$ of Gaofen-6, Sentinel-2, and Landsat-8 image were set equal to 125000, 100000, and 3300, and $AT_{\min}$ of Gaofen-6, Sentinel-2, and Landsat-8 image were set equal to 1000, 800, and 100, respectively. The unit of the numbers is pixels.

The $L_{\min}$ mentioned in Section III-D is used to remove the short line marks generated by HLT method. Considering the runway length and the scale of the category IV airports, the length threshold of Gaofen-6, Sentinel-2, and Landsat-8 image were set equal to 150, 120, and 40, respectively. The unit of the numbers is pixels.

The D_l of Gaofen-6, Sentinel-2, and Landsat-8 image mentioned in Section III-D were set equal to 400, 300, and 200, respectively. The unit of the numbers is pixels.

The value of F_{pix} mentioned in Section III-D is equal to 1250, 1000, and 400 pixels for the Gaofen-6, Sentinel-2, and Landsat-8 images, respectively.

2) Evaluation Metrics for Airport Detection: To evaluate the accuracy of airport detection, we applied a statistical analysis based on the number of airports detected. The analysis focuses mainly on the airports with concrete runways, although some airports included in the analysis have runways made of different materials in a single RSI. The overall detection rate (ODR), false alarm rate (FAR), and missing rate (MR) are used to quantitatively evaluate the airport detection results of the proposed method. The ODR, FAR, and MR are defined as follows:

$$ODR = \frac{d}{N} \times 100\% \quad (9)$$

$$FAR = \frac{f}{N_f} \times 100\% \quad (10)$$

$$MR = \frac{m}{N} \times 100\% \quad (11)$$

where d is the number of correctly detected airports, f is the number of airports that are incorrectly detected, m is the number of airports not detected at all, N_f is the total number of detected
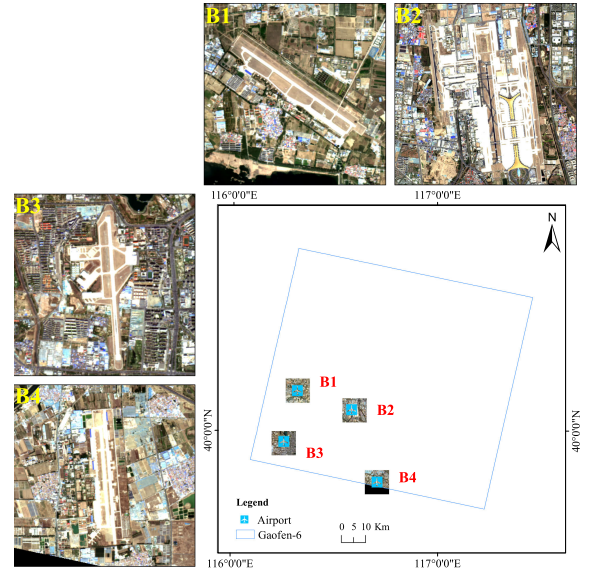

Fig. 14. Airport detection result based on whole scene Gaofen-6 image in BTH region.
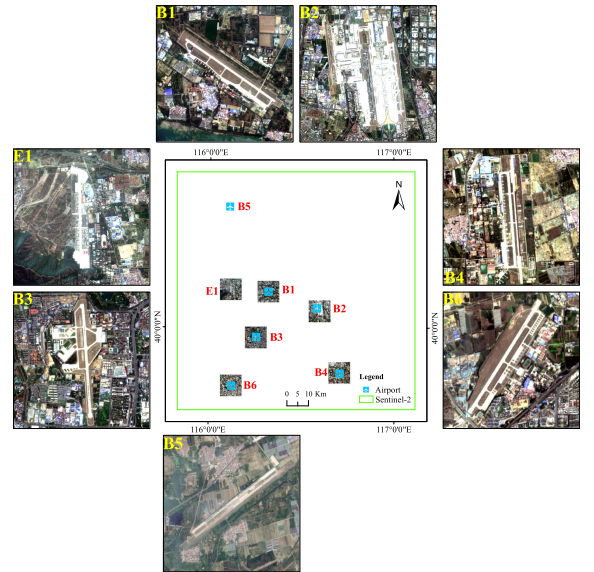

Fig. 15. Airport detection result based on whole scene Sentinel-2 image in BTH region.

objects, and N is the total number of airports in a whole scene RSI.

B. Airport Detection Result and Analysis

1) Airport Detection Result and Analysis Based on the RSIs With Different Spatial Resolutions: Figs. 14 –16 show the detected airports from the Gaofen-6, Sentinel-2, and Landsat-8 images, respectively. It can be seen from the airport detection result that all the airports are detected successfully based on the whole scene Gaofen-6 image. Most of the airports are detected successfully except B5 based on the whole scene Sentinel-2 image, and there is a detection error (E1). As for the whole scene Landsat-8 image, B2, B7, and B8 are detected successfully, but
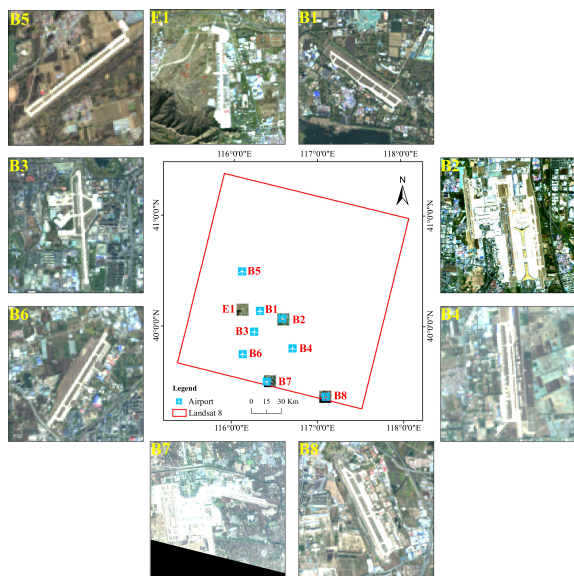
Fig. 16. Airport detection result based on whole scene Landsat-8 image in BTH region.

Fig. 17. Undetected airport.

B1, B3, B4, B5, and B6 are not detected, and have a detection error (E1), respectively.

Overall, the airport detection effect is worst based on the Landsat-8 image, while it is better based on the Gaofen-6 and Sentinel-2 images, which indicates that the airport detection is obviously affected by the image spatial resolution, i.e., the higher the spatial resolution, the better the airport detection effect. In addition, Sentinel-2 image can directly download L2A production, which can greatly save the overall processing time and cost. Combined with factors such as limit of image coverage and difficult of data acquisition, Sentinel-2 image is more suitable for airport detection than Gaofen-6 and Landsat-8 image.

Airport B5 [see Fig. 17(b)] was not detected in the Sentinel-2 images. In fact, the nearly 2300 m runway of B5 is longer than 1200 m (see Table I), that is, B5 is a category IV airport. In order to further analyses the causes, we collected another two scene Sentinel-2 images [see Fig. 17(c) and (d)] that acquired before (Mar. 23, 2020) and after (Nov. 8, 2020) the Sentinel-2 image used in this article. Through comparison, it is found that the main area of B5 airport runway is complete in the image acquired on Dec. 5, 2019 and Mar. 23, 2020. However, there are obvious bare soil areas rather than concrete areas marked by yellow straight line has obvious soil characteristics instead of concrete in May 12, 2020, which presents the signs of artificial reconduction. Moreover, the runway of B5 airport is much longer (the area marked by yellow circles) and brighter in Nov. 8, 2020, indicating that the airport runway reconstruction project is almost completed. All in all, the undetected airport is caused by the reason that the airport is still under reconstruction at the acquisition date of the image used in this article. Therefore, it is playing an important role in dynamically monitor changes of airport by establishing an effective airport detection method.

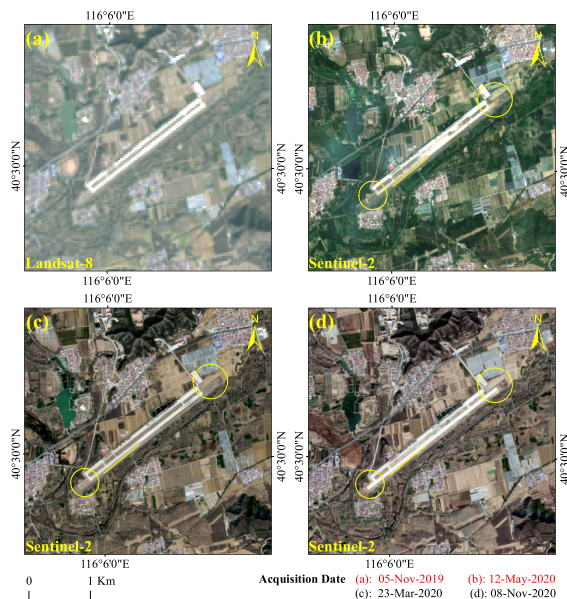There are many airports has not been detected successfully based on the Landsat-8 image, the reason is that low spatial resolution of the image causes the "boundary effect". Previous studies show that increased spatial resolution of images increases the spectral covariance, thereby reducing the pixel spectral separability and the "boundary effect" [47]. In fact, the runway of airport B5 is less than 50 m wide, which may produce a clearer boundary effect of Landsat-8 image than Gaofen-6 and Sentinel-2 image. And it affects the extraction of main concrete area by using the band decision tree method, so that the airport cannot be successfully detected.

In conclusion, the method proposed in this article has a good detection effect for Gaofen-6 and sentinel-2 images, and the higher image spatial resolution, the higher the accuracy of airport detection. In addition, the dynamic changes of the airport can be monitored effectively by airport detection.

2) Airport Detection Based on the Sentinel-2 Images With Different Background Complexity: Unlike the Gaofen-6 and Landsat-8 images, the Sentinel-2 image allows us to dispense with the complex, time-consuming preprocessing operations, which makes Sentinel-2 images the best choice of the three RSIs for airport detection. Due to the relatively scattered characteristics of airport spatial distribution, in order to further verify the accuracy of airport detection from Sentinel-2 images, we choose another eleven experimental areas and acquire the images with different background complexity. Appendix Figs. 18–28 show the airport detection results by applying the proposed method based on the whole scene Sentinel-2 images. Those areas contain a total of 30 airports with concrete runways, and all of them are category IV airports.

The results show that almost all the category IV airports with concrete runways are detected. Most incorrectly detected airports consist of runway-like targets [see Appendix Figs. 18(E1-E3), 19(E1), 20(E1), 22(E1), and 26(E1)], such as broad concrete roads, which present spectral characteristics similar to those of concrete airport runways, as well as similar linear features. In future research, open-source road vectors will be integrated into the proposed airport-detection method to prevent

concrete roads from being identified as airports. In addition, some airports are not detected successfully [see Appendix Figs. 18(B1), 18(B3), and 22(b3)], because the roof of a large number of artificial buildings are constructed of concrete around the airport, it is difficult to separate the building and the airport when extracting the main concrete area based on the decision tree method, so that the airport runway line marks cannot be effectively extracted by using HLT.

C. Comprehensive Evaluation of Airport Detection

1) Accuracy Evaluation of Airport Detection: Table V presents the statistical results for airport detection from Sentinel-2 images, and Table VI lists the overall accuracy of airport detection. There are 30 airports with concrete runways in the test areas, and 35 airports are detected from the airport detection result, including 27 detected correctly airports, 9 detected incorrectly airports, and 3 detected unsuccessfully airports. With the proposed method, the ODR and MR attain 90.00% and 10.00%, respectively, which shows that this method can be used to effectively detect category IV airports with concrete runways based on the whole scene RSIs.

2) Efficiency Evaluation of the Proposed Method: The proposed method provides airport detection integrated into a single MATLAB procedure. Given that each RSI has large data volume characteristics, the temporal efficiency of the proposed method should be further discussed. We, thus, compare the results of airport detection from Sentinel-2 images, which contain the most data of the three RSIs considered herein. Table VII shows the run-time of the proposed method applied to Sentinel-2 images of different locations. Almost all run-times are between 1 and 2 min. The processing time increases slightly of three different spatial resolution RSIs in BTH region.

3) Comparative Analysis of Airport Detection Efficiency: At present, there are few studies on using the whole scene RSIs as the processing unit or carrying out large-scale area to detect airports. Li *et al.* [19] constructed a framework for detection of unknown airports based on large-scale image by using Google image data (Level 17), combined with deep learning and geographic analysis, and choose the Jiangsu Province, Shanghai City, and Zhejiang Province as study area that cover a total area of $219\,040.5$ km^2. The overall processing time of the framework is 41762 s. In addition, the traditional manual visual search method was used to investigate the airports in the study area with a total processing time of 818535 s [19]. Therefore, in order to evaluate the processing efficiency between different methods, we take the area of 100 km^2 as the unit, and calculate the processing efficiency per unit area (s/one hundred square kilometers), the statistic results are shown in Table VIII. It shows that the processing efficiency of proposed method is about 16–32 times faster than Li *et al.* and about 300–600 times faster than that of the manual visual search method, which indicates that the proposed method is sufficiently rapid. It also indicated that the proposed method in this article has certain popularization and application.

V. CONCLUSION

In this article, we have proposed a feature fusion method to directly detect airports with concrete runways based on the whole
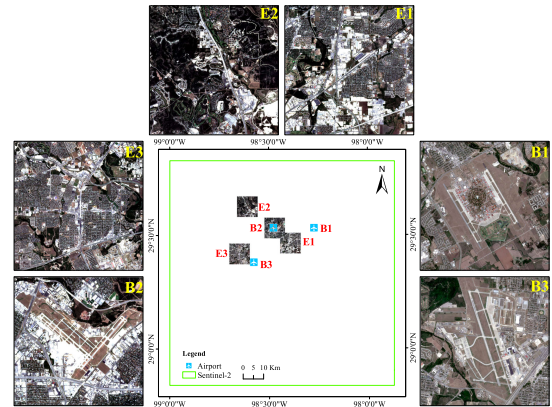

Fig. 18. Airport detection result based on the Sentinel-2 image within San Antonio area.

scene RSIs containing only blue, green, red, and NIR bands. And we apply the proposed method to Gaofen-6, Sentinel-2, and Landsat-8 RSIs to analysis the influence effect under different spatial resolution. In addition, we also apply the proposed method to Sentinel-2 images with different background complexity of experimental areas to verify the effectiveness of airport detection. The airport detection results and processing efficiency are then quantitatively evaluated and compared. The results of this article lead to the following main conclusions.

1) The proposed method is applied to the RSIs that containing only the blue, green, red, and NIR bands. On the one hand, we used the fewer bands to detect airports based on the complete RSIs. On the other hand, the remote sensing images of almost optical satellites commonly contain the mentioned four bands, which is relatively easy to access. By analyzing the spectral characteristics of different objects within the RSIs, we confirm that concrete areas within RSIs can be extracted based on proposed decision tree algorithm.
2) Airport detection is affected by the spatial resolution of RSIs. The higher the spatial resolution, the better the airport detection accuracy. And the Sentinel-2 images is more suitable for airport detection than Gaofen-6 and Landsat-8 images.
3) The proposed airport detection method has high robustness based on the whole scene Sentinel-2 images with different background complexity. And the results show that the proposed method has high accuracy. In addition, although the proposed method based on the whole scene RSIs, it also has high processing efficiency.

In the future work, we will continue to study enhance the precision of airport detection by combining road data with RSIs. In addition, there is a large amount of historical remote sensing image data could be processed based on the proposed method for monitoring airport dynamic change and timely updating relevant airport information database.

APPENDIX

The tables contain detailed description of the airports of experimental areas and the result figures of airport detection experimental are list in this section.
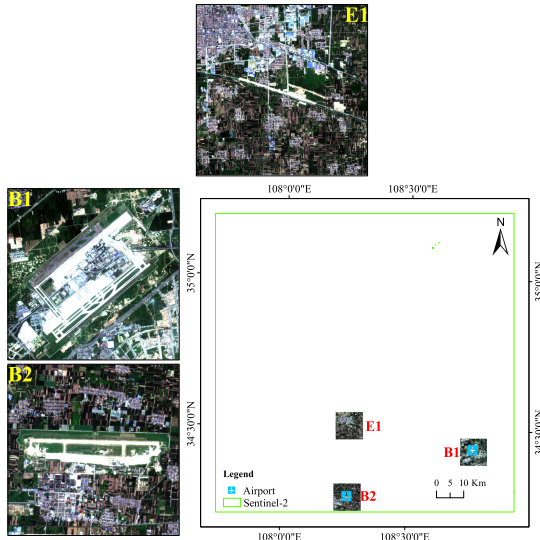
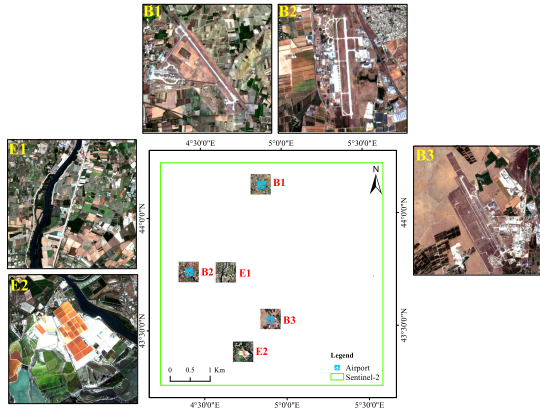Fig. 19. Airport detection result based on the Sentinel-2 image within xi'an area.

Fig. 20. Airport detection result based on the Sentinel-2 image within Marseille area.
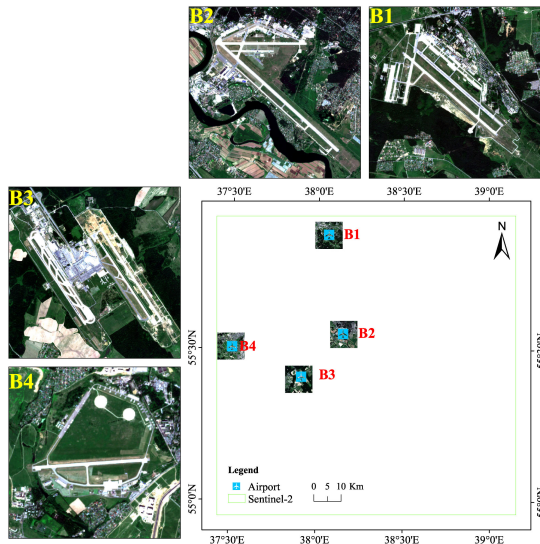

Fig. 21. Airport detection result based on the Sentinel-2 image within Moscow area.

TABLE IX
AIRPORT INFORMATION OF EXPERIMENTAL AREAS

| ID	Location	Number	Runway Material	Width of Runway (m)	Length of Runway (m)
1	BTH region	B1	Concrete	40	2600
			Asphalt	60	3800
		B2	Asphalt	50	3200
			Concrete	60	3800
		B3	Concrete	50	2500
		B4	Concrete	45	2200
		B5	Concrete	50	2600
		B6	Concrete	50	2400
			Concrete	60	3400
		B7	Concrete	60	3800
			Concrete	60	3800
			Concrete	45	3800
		B8	Concrete	60	2800
2	Moscow	B1	Concrete	100	3000
			Concrete	60	3600
		B2	Concrete	70	5400
			Concrete	50	3774
		B3	Concrete	70	3473
			Concrete	45	2668
		B4	Concrete	48	2052
3	Clinton County	B1	Concrete	46	3262
			Concrete	46	2744
4	Nouakchott	B1	Concrete	45	2400
			Concrete	60	3400
5	xi' an	B1	Concrete	60	3800
			Asphalt	45	3003
		B2	Concrete	55	3000
6	Beirut	B1	Concrete	45	2970
			Concrete	45	3802
		B2	Concrete	45	3389
			Asphalt	60	3218
		B3	Asphalt	45	2779
7	Marseille	B1	Concrete	60	2407
		B2	Concrete	45	2638
		B3	Concrete	60	3752
			Concrete	25	900
8	New York	B1	Concrete	46	4436
			Asphalt	61	2561
			Concrete	46	3462
9	St. Louis	B1	Concrete	46	3043
			Concrete	46	3048
			Asphalt	46	2438
		B2	Concrete	61	3355
			Concrete	46	2741
			Concrete	46	2740
			Concrete	46	2315
		B3	Concrete	46	2276
			Asphalt	23	1521
10	Minot	B1	Concrete	91	4015
		B2	Concrete	46	2344
			Asphalt	30	1930
11	Seattle	B1	Concrete	46	3628
			Concrete	46	2874
			Concrete	46	2591
12	San Antonio	B1	Concrete	61	2549
			Asphalt	61	2551
			Concrete	46	2593
		B2	Asphalt	30	1683
			Concrete	46	2290
		B3	Concrete	91	3531
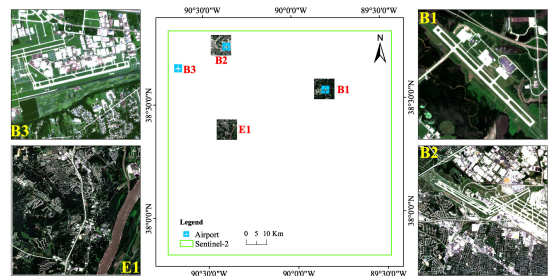
Fig. 22. Airport detection result based on the Sentinel-2 image within St. Louis area.
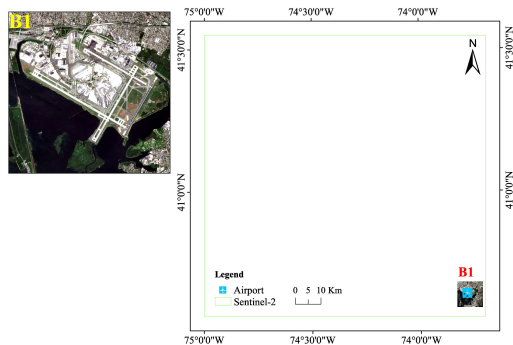
Fig. 23. Airport detection result based on the Sentinel-2 image within New York area.
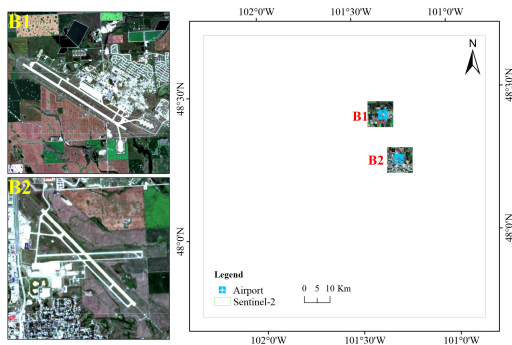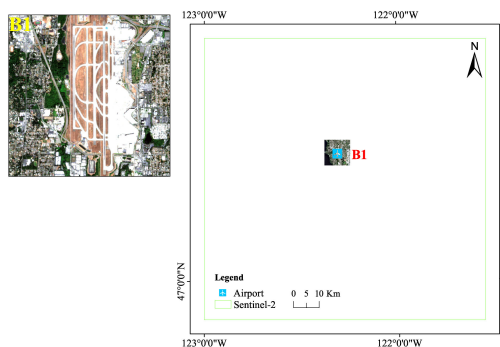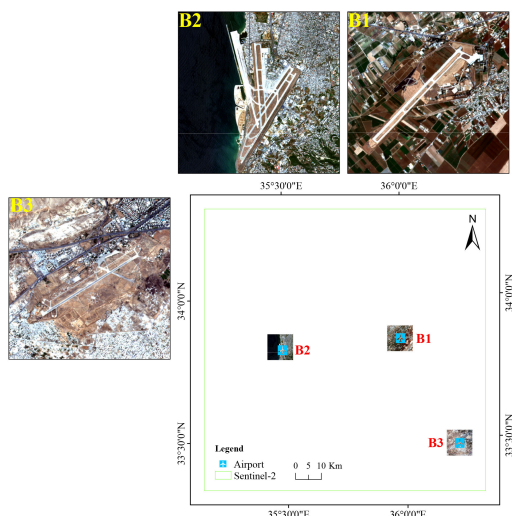

Fig. 24. Airport detection result based on the Sentinel-2 image within Seattle area.
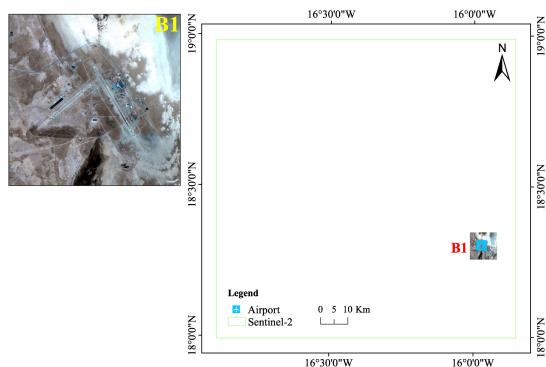

Fig. 25. Airport detection result based on the Sentinel-2 image within Nouakchott area.
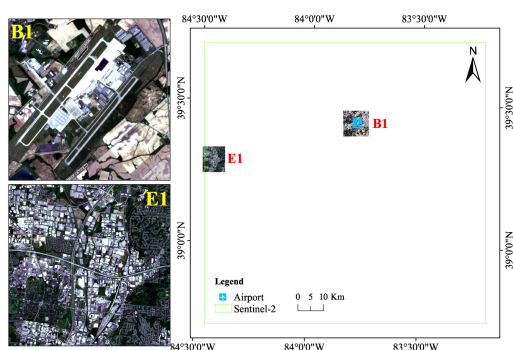

Fig. 26. Airport detection result based on the Sentinel-2 image within Clinton County area.

Fig. 27. Airport detection result based on the Sentinel-2 image within Minot area.

Fig. 28. Airport detection result based on the Sentinel-2 image within Beirut area.

REFERENCES

[1] G. Cheng and J. Han, "A survey on object detection in optical remote sensing images," *ISPRS J. Photogramm. Remote Sens.*, vol. 117, pp. 11–28, 2016.

[2] K. Li, G. Wan, G. Cheng, L. Meng, and J. Han, "Object detection in optical remote sensing images: A survey and a new benchmark," *ISPRS J. Photogramm. Remote Sens.*, vol. 159, pp. 296–307, Jan. 2020.

[3] Q. Zhang, L. Zhang, W. Shi, and Y. Liu, "Airport extraction via complementary saliency analysis and saliency-oriented active contour model," *IEEE Geosci. Remote Sens. Lett.*, vol. 15, no. 7, pp. 1085–1089, Jul. 2018.

[4] D. Zhu, B. Wang, and L. Zhang, "Airport target detection in remote sensing images: A new method based on two-way saliency," *IEEE Geosci. Remote Sens. Lett.*, vol. 12, no. 5, pp. 1096–1100, May 2015.

[5] L. Chen *et al.*, "A new framework for automatic airports extraction from SAR images using multi-level dual attention mechanism," *Remote Sens.*, vol. 12, no. 3, 2020.

[6] Z. Kou, Z. Shi, and L. Liu, "Airport detection based on line segment detector," in *Proc. Int. Conf. Comput. Vis. Remote Sens.*, Xiamen, China, 2012, pp. 72–77.

[7] X. Yao, J. Han, L. Guo, S. Bu, and Z. Liu, "A coarse-to-fine model for airport detection from remote sensing images using target-oriented visual saliency and CRF," *Neurocomputing*, vol. 164, pp. 162–172, 2015.

[8] U. Budak, U. Halici, A. Sengur, M. Karabatak, and Y. Xiao, "Efficient airport detection using line segment detector and fisher vector representation," *IEEE Geosci. Remote Sens. Lett.*, vol. 13, no. 8, pp. 1079–1083, Aug. 2016.

[9] B. Cai, Z. Jiang, H. Zhang, D. Zhao, and Y. Yao, "Airport detection using end-to-end convolutional neural network with hard example mining," *Remote Sens,* vol. 9, no. 11, 2017, Art no. 1198.

[10] D. Zhao, J. Li, Z. Shi, Z. Jiang, and C. Meng, "Subjective saliency model driven by multi-cues stimulus for airport detection," *IEEE Access*, vol. 7, pp. 32118–32127, 2019.

[11] A. Ludwig, H. Meyer, and T. Nauss, "Automatic classification of google earth images for a larger scale monitoring of bush encroachment in South Africa," *Int. J. Appl. Earth Obs. Geoinf.*, vol. 50, pp. 89–94, 2016.

[12] S. Zhang, Y. Lin, X. Zhang, and Y. Chen, "Airport automatic detection in large space-borne SAR imagery," *J. Syst. Eng. Electron.*, vol. 21, no. 3, pp. 390–396, 2010.

[13] W. Wang, L. Liu, C. Hu, Y. Jiang, and G. Kuang, "Airport detection in SAR image based on perceptual organization," in *Proc. Int. Work. Multiplatform/Multisensor Remote Sens. Mapping*, Xiamen, China, 2011, pp. 1–5.

[14] N. Liu, Z. Cui, Z. Cao, Y. Pi, and S. Dang, "Airport detection in large-scale SAR images via line segment grouping and saliency analysis," *IEEE Geosci. Remote Sens. Lett.*, vol. 15, no. 3, pp. 434–438, Mar. 2018.

[15] C. Tao, Y. Tan, H. Cai, and J. Tian, "Airport detection from large IKONOS images using clustered sift keypoints and region information," *IEEE Geosci. Remote Sens. Lett.*, vol. 8, no. 1, pp. 128–132, Jan. 2011.

[16] F. Chen, R. Ren, T. Van de Voorde, W. Xu, G. Zhou, and Y. Zhou, "Fast automatic airport detection in remote sensing images using convolutional neural networks," *Remote Sens,* vol. 10, no. 3, pp. 1–20, 2018.

[17] Y. Zhong, Z. Zheng, A. Ma, X. Lu, and L. Zhang, "COLOR: Cycling, offline learning, and online representation framework for airport and airplane detection using GF-2 satellite images," *IEEE Trans. Geosci. Remote Sens.*, vol. 58, no. 12, pp. 8438–8449, Dec. 2020.

[18] D. Liu, L. He, and L. Carin, "Airport detection in large aerial optical imagery," in *Proc. IEEE Int. Conf. Acoust. Speech Signal Process.*, Montreal, QC, Canada, 2004, pp. 12–15.

[19] N. Li *et al.*, "Framework for unknown airport detection in broad areas supported by deep learning and geographic analysis," *IEEE J. Sel. Topics Appl. Earth Obs. Remote Sens.*, vol. 14, pp. 6328–6338, Jun. 2021.

[20] Y. Qu, C. Li, and N. Zheng, "Airport detection base on support vector machine from a single image," in *Proc. 5th Int. Conf. Inf., Commun. Signal Process.*, 2005, pp. 546–548.

[21] D. Zhu, B. Wang, and L. Zhang, "Two-way saliency for airport detection in remote sensing images," in *Proc. Int. Conf. Audio, Lang. Image Process*, 2014, vol. 2, pp. 526–531.

[22] Z. C. Men, J. Jiang, X. Guo, L. J. Chen, and D. S. Liu, "Airport runway semantic segmentation based on DCNN in high spatial resolution remote sensing images," *Int. Arch. Photogramm. Remote Sens. Spatial Inf. Sci.*, vol. 42, no. 3/W10, pp. 361–366, 2020.

[23] Z. Xiao, Y. Gong, Y. Long, D. Li, X. Wang, and H. Liu, "Airport detection based on a multiscale fusion feature for optical remote sensing images," *IEEE Geosci. Remote Sens. Lett.*, vol. 14, no. 9, pp. 1469–1473, Sep. 2017.

[24] M. Sivaraja, "Installation of durable runway using firm concrete composite," *J. Adv. Civil Eng.*, vol. 2, no. 3, pp. 9–15, 2016.

[25] W. Lv, K. Dai, L. Wu, X. Yang, and W. Xu, "Runway detection in SAR images based on fusion sparse representation and semantic spatial matching," *IEEE Access*, vol. 6, pp. 27984–27992, 2018.

[26] X. Wang, Q. Lv, B. Wang, and L. Zhang, "Airport detection in remote sensing images: A method based on saliency map," *Cogn. Neurodynamic*, vol. 7, no. 2, pp. 143–154, 2013.

[27] D. Zhao, Y. Ma, Z. Jiang, and Z. Shi, "Multiresolution airport detection via hierarchical reinforcement learning saliency model," *IEEE J. Sel. Topics Appl. Earth Obs. Remote Sens.*, vol. 10, no. 6, pp. 2855–2866, Jun. 2017.

[28] L. Zhang and Q. Sun, "Saliency detection and region of interest extraction based on multi-image common saliency analysis in satellite images," *Neurocomputing*, vol. 283, pp. 150–165, 2018.

[29] T. Zhu, Y. Li, Q. Ye, H. Huo, and F. Tao, "Integrating saliency and resnet for airport detection in large-size remote sensing images," in *Proc. 2nd Int. Conf. Image, Vis. Comput.*, Chengdu, China, 2017, pp. 20–25.

[30] M. M. Zhu, Y. L. Xu, S. P. Ma, and H. Q. Ma, "Airport detection on remote sensing images using fater Region-based convolutional neural network," *J. Phys. Conf. Ser.*, vol. 1060, no. 1, 2018, Art. no. 012037.

[31] Y. Lecun, Y. Bengio, and G. Hinton, "Deep learning," *Nature*, vol. 521, no. 7553, pp. 436–444, 2015.

[32] L. Ma, Y. Liu, X. Zhang, Y. Ye, G. Yin, and B. A. Johnson, "Deep learning in remote sensing applications: A meta-analysis and review," *ISPRS J. Photogramm. Remote Sens.*, vol. 152, pp. 166–177, Jun. 2019.

[33] F. Zeng *et al.*, "A hierarchical airport detection method using spatial analysis and deep learning," *Remote Sens.,* vol. 11, no. 19, pp. 2204, 2019.

[34] International Civil Aviation Organization, "Aerodromes, Volume I: Aerodrome Design and Operations, (Annex 14 to the convention on International Civilian Aviation)," 4th ed. Montreal, QC, Canada, 2004.

[35] CASA, "Manual of standards: part 139 Aerodromes," Canberra, Australia: Civil Aviation Safety Authority, Sep. 2019.

[36] H. K. Zhang *et al.*, "Characterization of Sentinel-2A and landsat-8 top of atmosphere, surface, and nadir BRDF adjusted reflectance and NDVI differences," *Remote Sens. Environ.*, vol. 215, pp. 482–494, Sep. 2018.

[37] W. Liu, F. Baret, X. Gu, Q. Tong, L. Zheng, and B. Zhang, "Relating soil surface moisture to reflectance," *Remote Sens. Environ.*, vol. 81, no. 2/3, pp. 238–246, 2002.

[38] J. W. Rouse, R. H. Hass, J. A. Schell, and D. W. Deering, "Monitoring vegetation systems in the great plains with ERTS," *Third Earth Resour. Technol. Satell. Symp.*, vol. 1, pp. 309–317, 1973.

[39] S. K. McFeeters, "The use of the normalized difference water index (NDWI) in the delineation of open water features," *Int. J. Remote Sens.*, vol. 17, no. 7, pp. 1425–1432, 1996.

[40] N. R. Goodwin, L. J. Collett, R. J. Denham, N. Flood, and D. Tindall, "Cloud and cloud shadow screening across Queensland, Australia: An automated method for Landsat TM/ETM+ time series," *Remote Sens. Environ.*, vol. 134, pp. 50–65, 2013.

[41] Z. Zhu and C. E. Woodcock, "Automated cloud, cloud shadow, and snow detection in multitemporal landsat data: An algorithm designed specifically for monitoring land cover change," *Remote Sens. Environ.*, vol. 152, pp. 217–234, 2014.

[42] P. V. Hough, "A method and means for recognition complex patterns," U.S. Patent US3069654A, 1962.

[43] W. Liu, Z. Zhang, S. Li, and D. Tao, "Road detection by using a generalized hough transform," *Remote Sens.,* vol. 9, no. 6, 2017.

[44] A. A. Kassim, Z. Mian, and M. A. Mannan, "Connectivity oriented fast hough transform for tool wear monitoring," *Pattern Recognit,* vol. 37, no. 9, pp. 1925–1933, 2004.

[45] A. Scheer, H. Kruppke, and R. Heib, *Morphological Image Analysis: Principles and Applications*, 2nd ed. Berlin, Germany: Springer, 2004.

[46] F. G. B. De Natale and G. Boato, "Detecting morphological filtering of binary images," *IEEE Trans. Inf. Forensics Secur.*, vol. 12, no. 5, pp. 1207–1217, May 2017.

[47] P. F. Hsieh, L. C. Lee, and N. Y. Chen, "Effect of spatial resolution on classification errors of pure and mixed pixels in remote sensing," *IEEE Trans. Geosci. Remote Sens.*, vol. 39, no. 12, pp. 2657–2663, Dec. 2001.

Xinyu Dong received the B.S degree in spatial information and digital technology and the M.S. degree in agricultural resources and environment from Fujian Agriculture and Forestry University, Fuzhou, China, in 2015 and 2018, respectively. He is currently working toward the Ph.D. degree in geography with Nanjing University, Nanjing, China.

His research interests include remote sensing image processing and object detection on medium-high resolution remote sensing images.
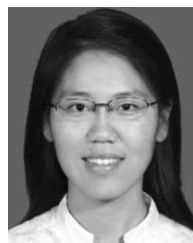
Jia Tian received the B.S. degree in electronic and information science from Nanjing University, Nanjing, Jiangsu, China, in 2012, and the M.S. and Ph.D. degrees in remote sensing from Cornell University, Ithaca, NY, USA, in 2016 and 2018, respectively.

She is currently a Postdoc Researcher with Nanjing University focusing on multi/hyperspectral remote sensing. Her research interests include radiative transfer modeling, spectral features of soil influenced by moisture content, identification of impervious surface, and nonphotosynthetic vegetation.

Qingjiu Tian received the B.S. degree in infrared from Shandong University, Jinan, China, in 1987, the M.S. degree in cartography and remote sensing from the Chinese Academy of Sciences, Beijing, China, in 1996, and the Ph.D. degree in cartography and geographical information system from Nanjing University, Nanjing, China, in 2003.

He is currently a Professor with the International Institute for Earth System Sciences, Nanjing University. His research interests include ground object detection and the retrieval of parameters by multi/hyperspectral remote sensing.